Supporting Information

Phase Modulation with Electrically Tunable Vanadium Dioxide Phase-Change Metasurfaces

Yonghwi Kim,[†] Pin Chieh Wu,[†] Ruzan Sokhoyan,[†] Kelly Mauser,[†] Rebecca Glaudell,[†] Ghazaleh Kafaie Shirmanesh,[†] and Harry A. Atwater[*†‡]

[†]Thomas J. Watson Laboratories of Applied Physics, California Institute of Technology, Pasadena, California 91125, United States
[‡]Kavli Nanoscience Institute, California Institute of Technology, Pasadena, California 91125, United States

*Corresponding author: Harry A. Atwater (haa@caltech.edu)

Contents

S1. VO_2 thin film growth and device fabrication

S2. VO_2 thin film characterization: electrical properties

S3. VO_2 thin film characterization: optical properties

S4. Full-wave simulation: electric field analysis

S5. Effective medium approximation

S6. Phase shift measurement optical setup

S7. Temporal response measurement

S1. VO_2 thin film growth and device fabrication

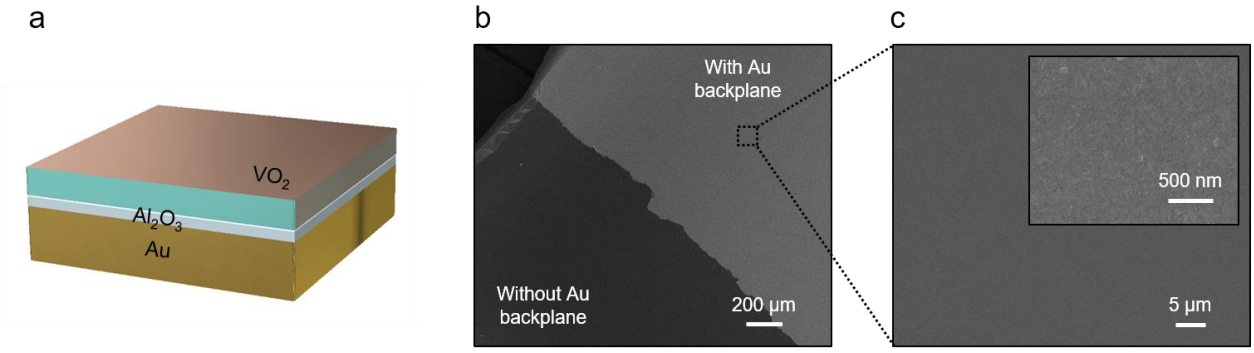


Figure S1. (a) Schematic of VO_2 thin film grown on the planar Au/Al_2O_3 heterostructure. The structure consists of a 40-nm–thick active VO_2 film, a 50-nm–thick Al_2O_3 layer, and an optically thick (150 nm) Au backplane. (b) Scanning electron microscope (SEM) image of the heterostructure structure and (c) the zoomed-in SEM image of the heterostructure with the Au backplane. The inset shows a further magnified SEM image of the continuous VO_2 film on the heterostructure, which was then patterned by the nanofabrication process.

The metasurface was fabricated on a cleaned fused silica substrate. First, a 150-nm–thick Au backplane was deposited on a 20-nm–thick Ti adhesion layer using electron beam deposition. Then a 50 nm Al_2O_3 layer was formed on top of the Au backplane by atomic layer deposition, followed by 40 nm of VO_2 formed by pulsed layer deposition (at 650 °C in a 5-mTorr O_2 environment), which resulted in a heterostructure as shown in Figure S1a. Scanning electron microscope images of the planar heterostructure are shown in Figure S1b,c. We verified that during the growth processes the surface of the heterostructure was smooth and without cracks that could lead to the failure of the device's electrical control due to the leakage current.[1] The metasurface pattern was written on the positive electron-beam resist using electron-beam lithography, and the pattern was developed in a resist developer. A 40-nm–thick Au layer and a 10-nm–thick Cr layer were then deposited consecutively on the developed resist using electron beam deposition. This was followed by a lift-off process to form the designed patterns. The patterned top metal layer (Cr) was subsequently used as a hard mask for the dry etching of the VO_2 layer with a fluorine-based inductively coupled plasma-reactive ion etching (ICP-RIE) process, which yielded self-aligned metal-insulator-metal antenna arrays. Finally, the Cr mask was removed by a brief dry etching process, using a chlorine-based ICP-RIE process.

S2. VO_2 Thin film characterization: electrical properties

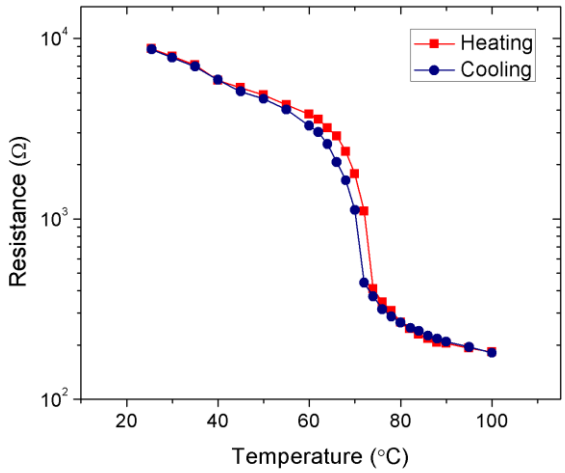


Figure S2. Electrical resistance hysteresis curves of the VO_2 thin film grown on the planar Au/Al_2O_3 heterostructure formed on a fused silica substrate. The resistance was measured based on the van der Pauw method during heating/cooling cycles, where the temperature was controlled by a thermoelectric element.

We adopted van der Pauw method to measure the electrical resistance of the VO_2 film grown on the planar Au/Al_2O_3 heterostructure formed on the fused silica substrate (Figure S1a). The temperature-dependent resistance was recorded by applying heating/cooling temperature cycles in the 25–100 °C range where the temperature was controlled by a thermoelectric element. Figure S2 shows the temperature-dependent hysteresis of the resistance for a 40-nm–thick VO_2 film. We observed a drastic change in the resistance as the samples' temperatures passed the insulator-to-metal (IMT) transition temperature, which is around 68 °C.

S3. VO_2 Thin film characterization: optical properties

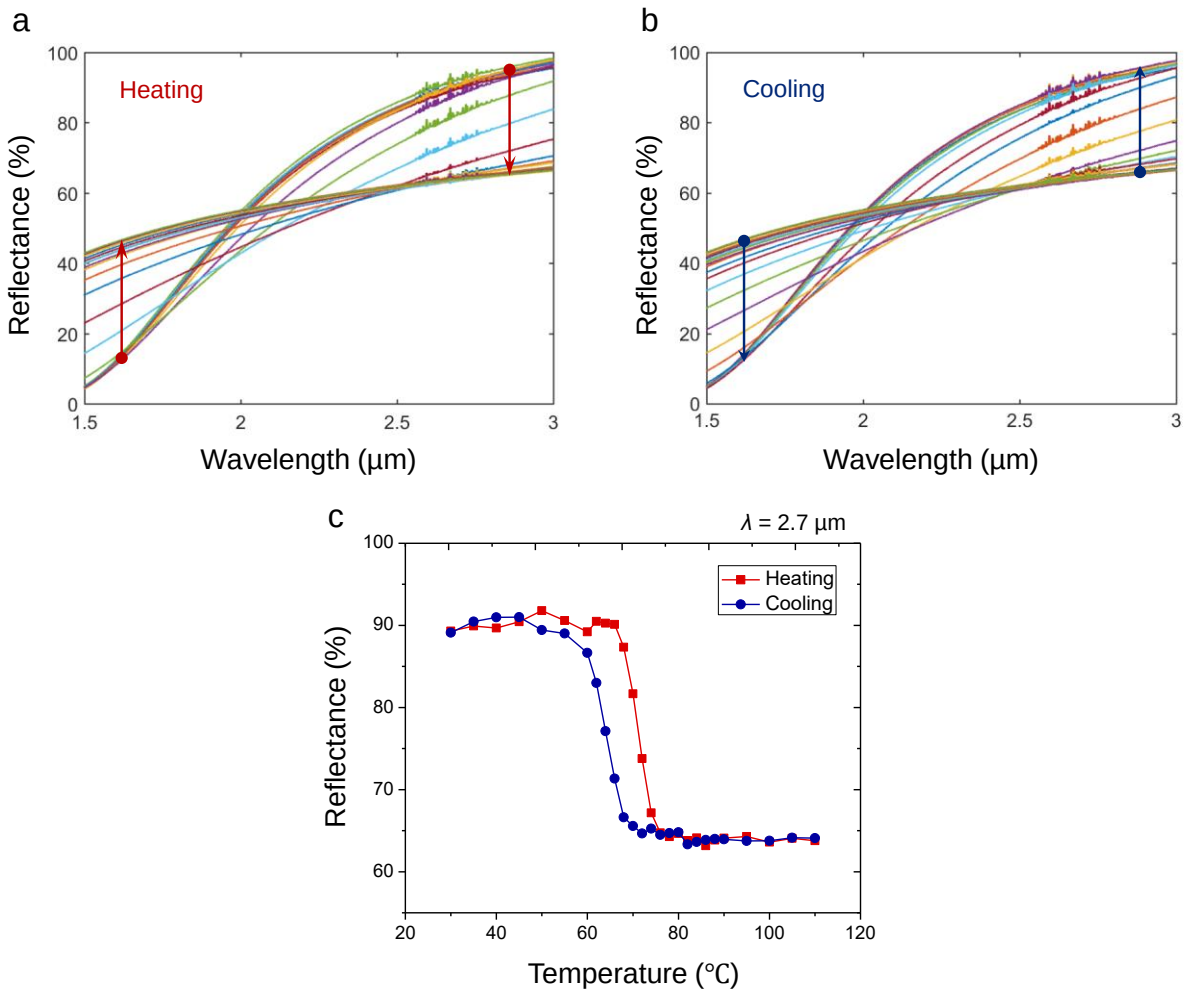


Figure S3. Temperature-dependent reflectance of a VO_2 film during (a) the heating cycle and (b) the cooling cycle. (c) Hysteresis cycle at λ = 2.7 μm extracted from figures (a) and (b), showing a sharp and reversible reflectance across the phase transition in the VO_2 thin film.

In order to characterize the optical properties of the VO_2 films grown on the planar Au/Al_2O_3 heterostructure (Figure S1a) across the IMT, we measured the optical reflectance curves in the near- and mid-infrared ranges as a function of temperature. Figure S3a and S3b represent the temperature-dependent reflectance modulation in the 27–110 °C range of a 40-nm–thick VO_2 film for heating and cooling cycles, respectively. We observed that the temperature-dependent optical reflectance changes significantly across the IMT. Based on the temperature-dependent reflectance data shown in Figures S3a and S3b, we represent in Figure S3c the reflectance as a function of temperature at λ = 2.7 μm. We observed the thermal hysteresis of the reflectance as similar to the one in Figure S2.

S4. Full-wave simulation: electric field analysis

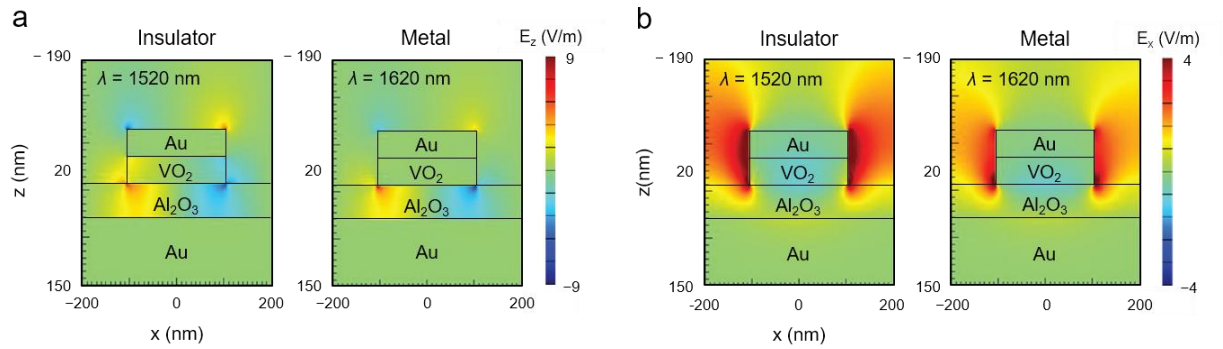


Figure S4. Electric field distribution of the metasurface structure. (a) Spatial distribution of the z component of the electric field E_z. (b) Spatial distribution of the x component of the electric field E_x. The left panels of each figure indicate the insulating phase resonance (λ = 1520 nm), while the right panels indicate the metallic phase resonance (λ = 1620 nm).

We used finite-difference time-domain methods to simulate the periodic antenna structure under normal incidence illumination with a transverse magnetic plane wave. In Figure 2b shows the existence of concentrated magnetic field magnitude $|H_y|$ in the dielectric gap of antenna elements as a result of a magnetic dipole resonance. Figure S4a shows the enhanced z component of the electric field E_z around the right and left edges of the antenna, which are antiparallel to each other. Figure S4b also shows the existence of an antiparallel x component of the electric field E_x around the top (light blue) and bottom (light yellow) of the dielectric gaps, which indicates an antiparallel electric field as a result of the magnetic dipole resonance. As seen in the right panels of Figure S4a and S4b, the electric fields become more localized in the Al_2O_3 layer as the VO_2 layer undergoes an insulator-to-metal transition. The tendency is consistent with the change in the magnetic field magnitude distributions of Figure 2b as a result of perturbation in the magnetic dipole resonance.

S5. Effective medium approximation

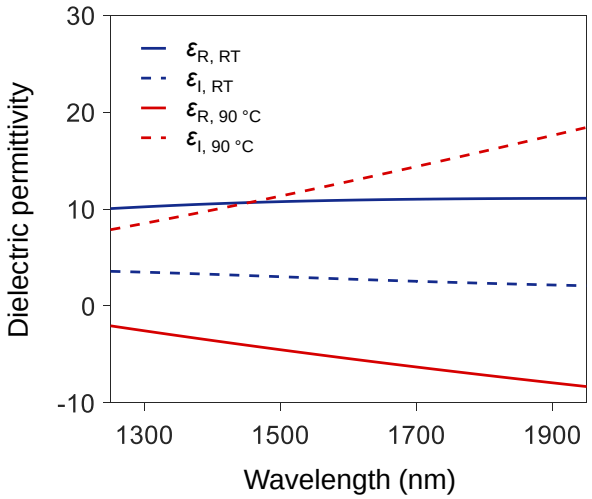


Figure S5. Measured dielectric permittivity of a VO_2 thin film on a sapphire substrate at RT and 90 °C, which clearly indicates the phase transition. The real part of the dielectric permittivity of VO_2 (solid line) changes its sign from positive to negative upon phase transition.

To estimate the effective optical constants of the VO_2 layer that were used in the full-wave electromagnetic simulation, we employed the Bruggeman effective medium approximation. The effective complex optical constants $\tilde{\varepsilon}_E(\omega)$ of a two-component system in the Bruggeman model for generalized ellipsoidal inclusions is given by

$$f\frac{\tilde{\varepsilon}_r(\omega)-\tilde{\varepsilon}_E(\omega)}{\tilde{\varepsilon}_r(\omega)+\frac{(1-q)}{q}\,\tilde{\varepsilon}_E(\omega)}+(1-f)\frac{\tilde{\varepsilon}_m(\omega)-\tilde{\varepsilon}_E(\omega)}{\tilde{\varepsilon}_m(\omega)+\frac{(1-q)}{q}\,\tilde{\varepsilon}_E(\omega)}=0$$

where $\tilde{\varepsilon}_r(\omega)$ and $\tilde{\varepsilon}_m(\omega)$ are the wavelength-dependent complex optical constants of the rutile and monoclinic phases, respectively as shown in Figure S5, f is the volume fraction of the rutile phase, and q is the depolarization factor that depends on the shape of the inclusions. The depolarization factor is chosen based on the assumption that the rutile phase inclusions are spherical at low concentration, and it continuously increases assuming that the rutile phase inclusions form disk shapes at higher concentrations.[2]

S6. Phase shift measurement optical setup

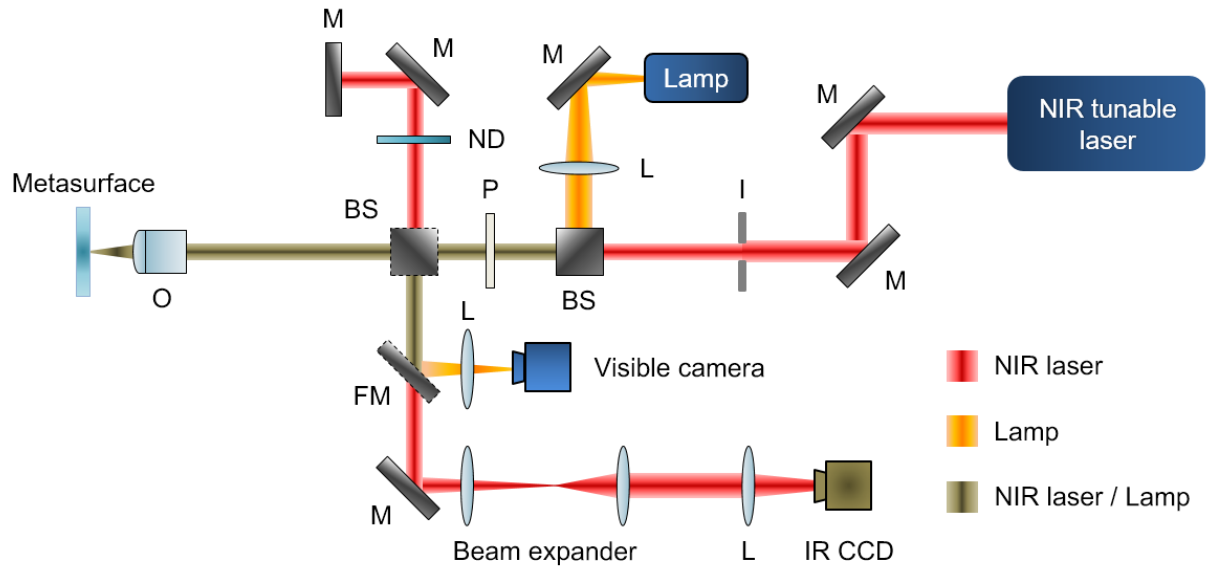


Figure S6. Schematic of the optical setup for the phase shift measurement. The labels of each optical component refer to the following: M (mirror); I (iris); BS (beam splitter); L (lens); P (linear polarizer); ND (neutral-density filter); FM (flip mirror).

The interference fringes of reflected light from the metasurface (Figure 4a) are measured by a Michelson-type interferometer, as shown in Figure S6. A tunable near-infrared light source is directed onto a 50/50 beam splitter after passing through a linear polarizer. We used a white light source and a visible camera to position the incident beam on the metasurface structures. One beam was focused onto a reference mirror, while the other beam was focused at the edge of the metasurface structures to utilize the planar Au/Al_2O_3 heterostructure as a phase reference. By using an infrared CCD camera, we recorded interference fringes formed by the interference from the reference mirror's beam and by the sample beam from the metasurface. We post-processed the captured interference images as a function of applied bias to analyze the phase shift of reflected light, as described in the main text.

S7. Temporal response measurement

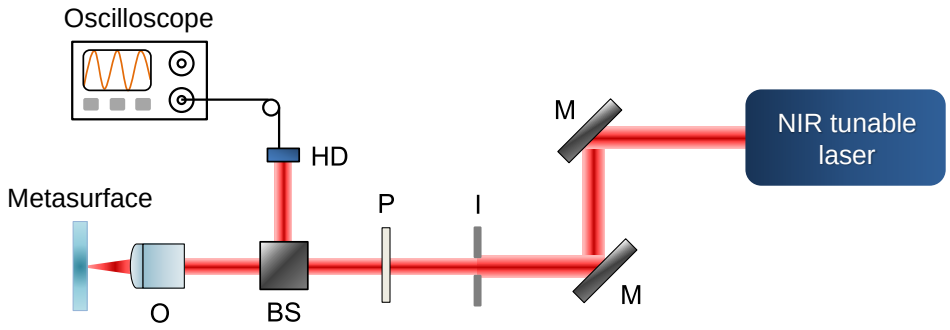


Figure S7. Schematic of the optical setup for the temporal response measurement. Here HD refers to a high-speed InGaAs detector.

We measured the device's temporal response using a function generator to modulate the reflected signal when rectangular voltage pulses were applied. The reflected signal at 1550 nm was monitored using an oscilloscope (Figure S7). Figure S8 presents the results when we applied 2.5-s–wide and 50% duty-cycle electrical voltage pulses for different peak-to-peak voltages. First, when the applied bias was 3.4 V_{pp} (Figure S8a), there was no observable change in the reflected signal, indicating that the applied bias was below the transition threshold (Figure 3c). We observed a decrease in the reflected signal as we increased the bias to 8.9 V_{pp} (Figure S8b). The reflected signal decreased further and reached its minimum when the bias was decreased to 9.3 V_{pp} (Figure S8c), and it saturated when the bias was 10.9 V_{pp} (Figure S8d), indicating that the VO_2 had completely switched to the rutile phase. We noted that the monitored non-monotonic behavior corresponds to the steady-state responses as shown in Figure 3c. At fixed wavelength (λ = 1550 nm), the reflected signal shows a non-monotonic behavior because of the redshift of the resonance dip when the applied bias is larger than 8.9 V_{pp}.

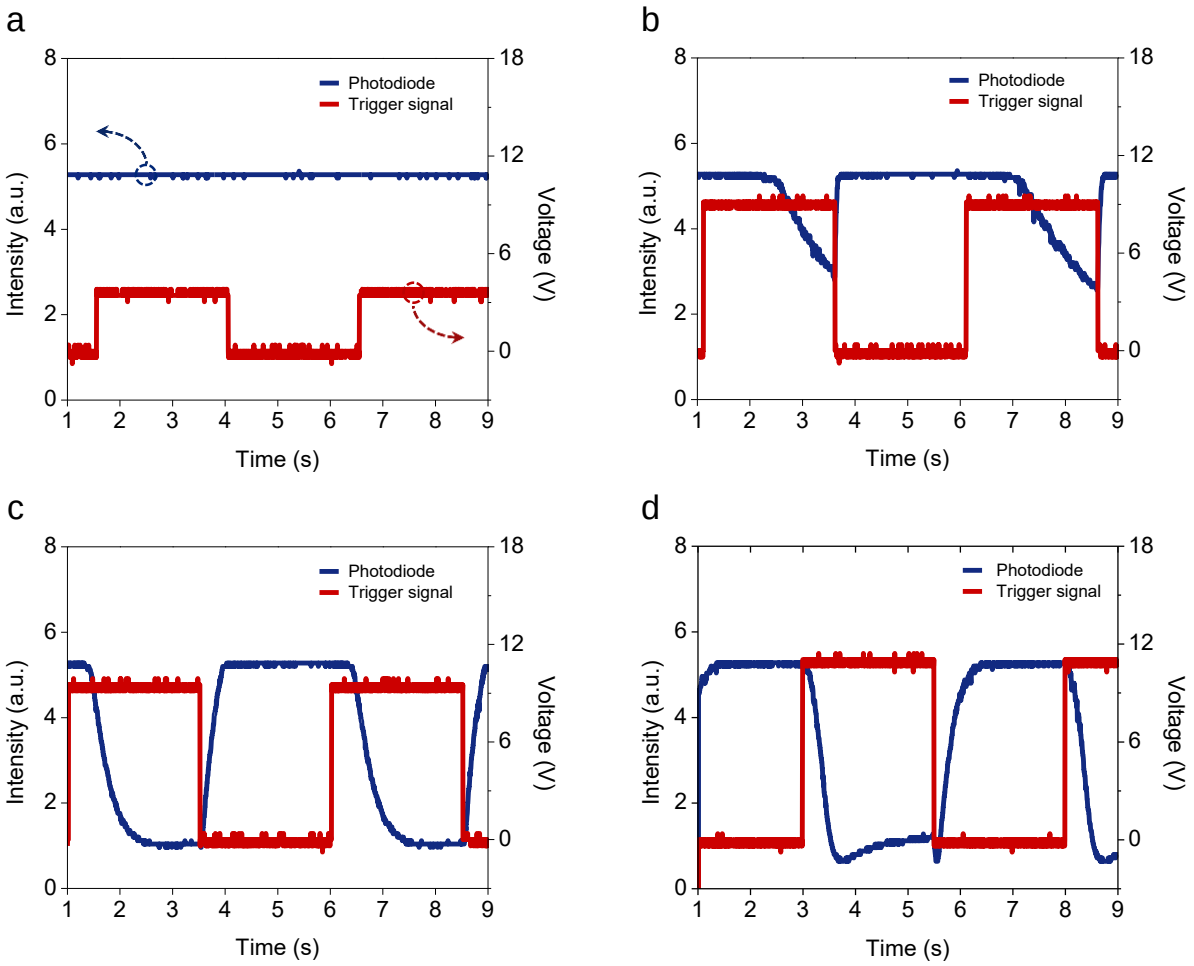


Figure S8. Temporal response of the metasurface for different peak-to-peak voltages. The corresponding peak-to-peak voltages are (a) 3.4 V_{pp}, (b) 8.9 V_{pp}, (c) 9.3 V_{pp}, and (d) 10.9 V_{pp}, respectively. In the figures, the blue and red lines correspond to reflected signals at λ = 1550 nm and trigger signals (voltage pulses), respectively.

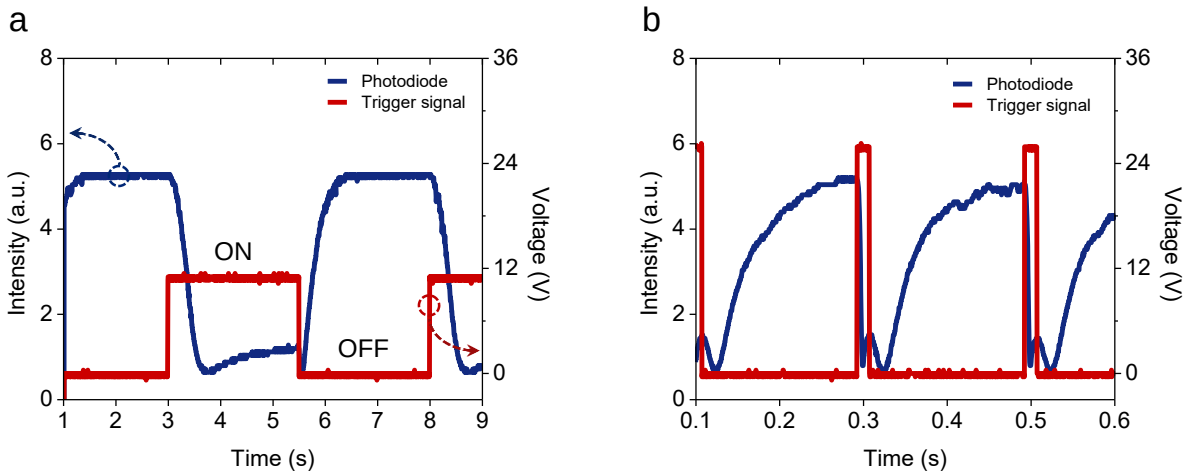


Figure S9. Temporal response of the metasurface for different applied voltage pulses. (a) Reflected signal for 10.9 V_{pp}-high and 2.5-s–wide voltage pulses with a 50% duty cycle. (b) Reflected signal for 25.7-V_{pp}–high and 15-ms–wide voltage pulses with a 7.5% duty cycle.

The measured ON and OFF switching time (complete phase transition) for the biases with 10.9-V_{pp}–high, 2.5-s–wide, and 50% duty-cycle voltage pulses were ≈ 2 s and ≈ 700 ms, respectively (Figure S9a). However, the switching speed is not limited by the intrinsic transition speed of the VO_2, but mainly by the thermal design of the device and input parameters. We noted that the previously reported switching speeds, involving thermal processes, are sub-picosecond for optical excitation[3] and a few nanoseconds for electrical switching.[4] Nevertheless, the switching speed of the metasurface can be significantly enhanced by utilizing more-localized Joule heating, by manipulating applied electrical pulses.[5] For example, we observed ON and OFF switching times of ≈ 15 ms and ≈ 100 ms, respectively, by applying high-intensity (25.7 V_{pp}) short (15 ms) voltage pulses with a 7.5% duty cycle, as shown in Figure S9b.

References

(1) Zhu, Z.; Evans, P. G.; Haglund, R. F.; Valentine, J. G. *Nano Lett.* **2017**, *17* (8), 4881–4885.

(2) Qazilbash, M. M.; Brehm, M.; Chae, B.-G.; Ho, P.-C.; Andreev, G. O.; Kim, B.-J.; Yun, S. J.; Balatsky, A. V.; Maple, M. B.; Keilmann, F.; et al. *Science* **2007**, *318* (5857), 1750–1753.

(3) Liu, M.; Hwang, H. Y.; Tao, H.; Strikwerda, A. C.; Fan, K.; Keiser, G. R.; Sternbach, A. J.; West, K. G.; Kittiwatanakul, S.; Lu, J.; et al. *Nature* **2012**, *487* (7407), 345–348.

(4) Markov, P.; Marvel, R. E.; Conley, H. J.; Miller, K. J.; Haglund, R. F.; Weiss, S. M. *ACS Photonics* **2015**, *2* (8), 1175–1182.

(5) Liu, L.; Kang, L.; Mayer, T. S.; Werner, D. H. *Nat. Commun.* **2016**, *7*, 13236.